Spin transport and superconductivity in half-metallic nanowires and junctions

Yao, J.

Citation

Yao, J. (2023, July 5). *Spin transport and superconductivity in half-metallic nanowires and junctions*. *Casimir PhD Series*. Retrieved from https://hdl.handle.net/1887/3629768

5

Triplet Supercurrents in Lateral Josephson Junctions with a Half-metallic Ferromagnet

Spin triplet supercurrents in half-metallic ferromagnets (HMFs) would be a valuable addition to the toolbox of superconducting spintronics since they promise to be long-range, fully spin-polarized, and with high current density. However, experimental studies on the subject remain scarce because there are only few HMFs available. Here we report on the generation of triplet supercurrents in mesoscopic lateral Josephson junctions, fabricated with the conventional superconductor NbTi and the HMF $La_{0.7}Sr_{0.3}MnO_3$ *(LSMO), having a typical junction length of 20 nm. We use the electrode geometry as a tool to examine the triplet generator in the HMF and study junctions shaped as bar, square, and disk. In all junctions, we find strong supercurrents and high current densities, that are independent of the junction geometry and are insensitive to the application of in-plane fields, ruling out the magnetic vorticity in the disk geometry as the generator. Analysis of the critical current interference pattern upon application of a perpendicular magnetic field shows that the triplet supercurrent is highly constricted to the rims of the disk devices, yet uniformly distributed in the bar-shaped devices. The appearance of these rim*

The adapted version of this chapter has been submitted to a peer-reviewed journal by Yao Jungxiang, Remko Fermin, Kaveh Lahabi, and Jan Aarts.

supercurrents is tied to the combination of triplet transport and the disk geometry but is not central to the generator mechanism. Next, we analyze the temperature dependence of the critical current and find in its quadratic dependence a strong indication for the triplet nature of the supercurrents. Finally, we find the supercurrent to persist in junctions fabricated from a NbTi/Ag/LSMO trilayer. The results strongly indicate that the magnetic inhomogeneity needed for triplet generation resides in the LSMO layer adjacent to the NbTi/LSMO interface.

5.1. Introduction

Arguably the most promising ferromagnetic (F) materials for superspintronics applications are the half-metallic ferromagnets (HMF), such as CrO_2 and the metallic oxide perovskites $La_{0.7}X_{0.3}MnO_3$ (X = Sr (LSMO); or Ca (LCMO)) [10, 11, 147]. Despite their fully spin-polarized nature, both in CrO_2 and in the metallic oxide perovskites long-range triplet (LRT) proximity effect was found, showing high critical currents, and superconducting proximity over extremely long length scales [14, 69, 70, 148]: in CrO_2 over a distance of almost 0.5 μm and in LSMO even bridging 1 μm [14, 149]. However, the mechanism that converts singlets in the superconductor (S) to triplets in the HMF - regardless of whether it concerns CrO_2 or the manganite oxides - is still poorly understood. This is contrary to LRT generation in conventional S/F systems, where a spin-active interface is engineered at which spin mixing and spin rotation processes conspire to the formation of equal-spin triplet correlations [72, 150]. Stack of magnets with non-collinear magnetizations are generally used for the magnetic inhomogeneity [74, 151, 152]. More recently, magnetic vortices [51, 62, 153, 154], domain walls [155–158], and spin-orbit coupling [159–166] were also identified as triplet generators, but they do not explain the results on HMFs. The results on CrO_2 without engineered magnetic non-collinearity are hypothesized to result from intrinsic strain-induced magnetic inhomogeneity or grain boundary disorder [167], but there are no established sources of LRT correlations in the recent experiments on LSMO junctions [14]. Therefore, the intrinsic mechanism for triplet generation in LSMO remains a major open question.

Here we study the generation of LRT correlations in junctions of LSMO and NbTi, which is a conventional s-wave superconductor with a relatively low transition temperature (~ 7.5 K in this work) and qualitatively different from the high-T_c and d-wave superconductor YBCO used in previous experiments. Inspired by previous work [51] where we showed that a magnetic vortex is capable of generating spin-polarized supercurrents, we use geometry as a tool to examine the role of spin texture in LRT generation (see Fig. 5.1). We fabricated lateral junctions with disk, square, and bar shapes. We find high critical currents in our devices, which we identify as triplet supercurrents, by examining their temperature dependence. Unexpectedly, the triplet supercurrents occur irrespective of the device geometry, a result that rules out spin texture as the LRT generator. However, the current distribution in both devices is quite different. Analysis of the critical current interference patterns upon application of a perpendicular magnetic field shows that in the disk, the supercurrent is highly constricted to its rims, similar to results we obtained on disk junctions made of Nb/Co [51]. For the bars we find a homogeneous distribution over its cross-section. The results show that the triplet generator mechanism and the origin of these *rim supercurrents* in our HMF/NbTi disks

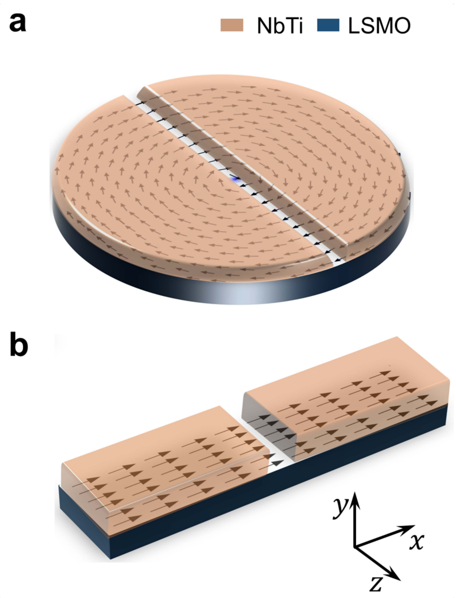

Figure 5.1: Schematic illustration of NbTi/LSMO junctions of different geometry. (a) A disk-shaped junction consisting of NbTi (orange) and LSMO (blue). Due to the shape anisotropy, a stable magnetic vortex forms in the LSMO layer, as indicated. (b) A bar-shaped junction with a uniform magnetic texture. The $x(z)$-axis is perpendicular (parallel) to the trench (both in the sample plane). The out-of-plane direction is the y-axis.

are not the same. Finally, we find the supercurrents unaltered in samples fabricated from a NbTi/Ag/LSMO trilayer, thereby ruling out any LRT sources resulting from an emerging interfacial magnetism due to exchange interactions across the NbTi/LSMO interface. We conclude that there is a generator at play due to an intrinsic magnetic inhomogeneity in the LSMO at, or close to, the LSMO/NbTi interface.

5.2. Results

Josephson junction devices were fabricated from bilayers of 60 nm NbTi deposited on 40 nm LSMO grown on an $(LaAlO_3)_{0.3}(Sr_2TaAlO_6)_{0.7}$ (LSAT) substrate. Samples were structured by Focused Ion Beam (FIB). We fabricated disk, square, and bar geometries, the latter with two different aspect ratios (length-between-contacts to width) of 3:1 and 5:1. The typical dimension of all structures was 1 μm. Also by FIB, a trench was made in the middle of the devices. The trench width corresponds to the junction length. All junctions in this work have an identical length of d ~ 20 nm. More details on the device fabrication can be found in the Methods section 5.5.1 in Appendix 5.5.

The resistance R of the differently shaped NbTi/LSMO junctions was measured as a function of temperature T, as shown in Fig. 5.2a. The normal state resistance for all de-

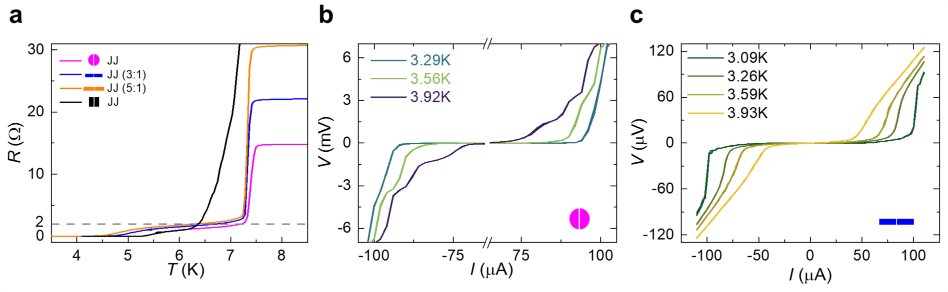

Figure 5.2: Electrical transport. (a) Resistance versus temperature curves for disk-shaped (magenta), square-shaped (black), bar-shaped 3:1 (blue), and 5:1 (orange) devices. The grey dashed line is a guide to the eye at 2 Ω. (b) A plot of current (I) - voltage (V) curves taken at different temperatures on the disk-shaped junction. (c) Measured IV curves on the bar-shaped (3:1) junction at different temperatures.

vices is around 20 Ω, except for the square one which is 75 Ω, due to a different contact geometry. The traces show two transitions with decreasing temperature. The first one corresponds to the superconducting transition of NbTi at $\sim$ 7.5 K, and is followed by a plateau, which corresponds to the resistance of the LSMO weak link. As the temperature further decreases, the resistances fully go to zero, with broad tails, indicating that the weak links become superconducting in all junctions, regardless of their geometry and aspect ratio. Since LSMO is a half-metal, the proximity effect must be carried by LRT correlations.
In Fig. 5.2 we also show current I versus voltage V (IV-characteristics) for different temperatures of the disk-shaped and the (3:1) bar-shaped junctions, measured by sweeping the current back and forth. The data clearly show the onset of voltage at the critical current I_c, without visible hysteresis. The multiple steps in the IV curves of the disk junction at higher temperatures result from destroying superconductivity in nanostructured regions in the junction.

As mentioned, previous work on Nb/Co devices found proximity supercurrents in disk junctions, resulting from the spin texture of the device. Nb/Co-based bar-shaped junctions were never superconducting due to their uniform magnetization. In the case of LSMO-based junctions, we find a temperature-dependent I_c for all junctions, regardless of the device geometry.

5.2.1. Spatial supercurrent distribution

To study the relative distribution of critical currents along the junction, we examined the superconducting quantum interference, *i.e.* we recorded $\mathrm{I}_c(\mathrm{B}_\perp)$-patterns of the differently shaped junctions at 4.1 K (disk and square) and 3.5 K (3:1 bar). The results (see Fig. 5.3d-f) show a clear dependence on the sample geometry. For the disk, the

$I_c(B_\perp)$-pattern is two-channel-like, where the side lobes have a period comparable to the central peak, and the $I_c(B_\perp)$ oscillations decay gradually and less fast than the $1/B_\perp$ behavior expected for a single junction. This points to the existence of two superconducting channels in the disk-shaped NbTi/LSMO junction. Contrarily, for the bar (aspect ratio 3:1), we find a typical single-junction Fraunhofer-like pattern. The square-shaped junction is somewhat in between. We extracted the periodicity for each pattern by using a voltage criterion (see 5.5.4 in Appendix 5.5). In the case of the disk-shaped junction, the width of the central peak is about 5.91 mT, and that of the first lobe is about 5.04 mT, yielding a ratio of ~ 1.17. For the square-shaped and bar-shaped junctions, we obtain ratios of ~ 1.37 and ~ 1.45, respectively. The difference may be intrinsic in these junctions or correlated with the magnetic structures, as we will discuss later.

To convert the $I_c(B_\perp)$-pattern into the spatial distribution of the critical supercurrent, we employ a Fourier method and reconstruct the supercurrent density along the z axis (along the trench) [51, 52, 168]. The analysis requires the effective junction length L_{eff}, which is often taken as $L_{eff} = d+2\lambda_L$. Since the thickness of NbTi electrodes (60 nm) is smaller than their London penetration depth (λ_L; of order 0.5 µm), we adopt the universal limits $L_{eff} = (1/3.8) * L, (1/2.5) * L, (1/1.842) * L$ for the disk-shaped, square-shaped and bar-shaped junctions, respectively, where $L \approx 1.3\ \mu m$ is the junction width [52]. We find the supercurrents to be largely constricted to the rims of the device in the disk-shaped LSMO junction (Fig. 5.3h). This is similar to the disk-shaped Nb/Co junctions, although the width of the channels is larger (measured by the full width at half maximum ~200 nm). However, as the geometry of the junction changes from disk to square to bar (Fig. 5.3i and j), the density of supercurrent in the middle regions becomes more and more pronounced (Fig. 5.3h-j). Notably, the control experiment on disk-shaped MoGe/Ag junction also proves singlet supercurrents are distributed homogeneously across the trench, rather than being localized at the rim [51].

5.2.2. The effect of in-plane fields on the supercurrent distribution

In Nb/Co disk junctions, we found that the proximity effect, and in particular the rim supercurrents, were a consequence of the spin vortex texture. Therefore, the transport characteristics of the device are very sensitive to the exact spin texture of the weak link, for example by moving the vortex core using an in-plane (IP) field. In order to explore the similarity, we apply IP fields on the NbTi/LSMO disk junction to change the magnetic ground state, which is also a magnetic vortex (according to micromagnetic simulations; details in Methods 5.5.1). The results are shown in Fig. 5.4. Surprisingly, we find no change in the critical current while applying an IP field. Moreover, the $I_c(B_\perp)$-patterns persist, both when IP fields are applied perpendicular or parallel to

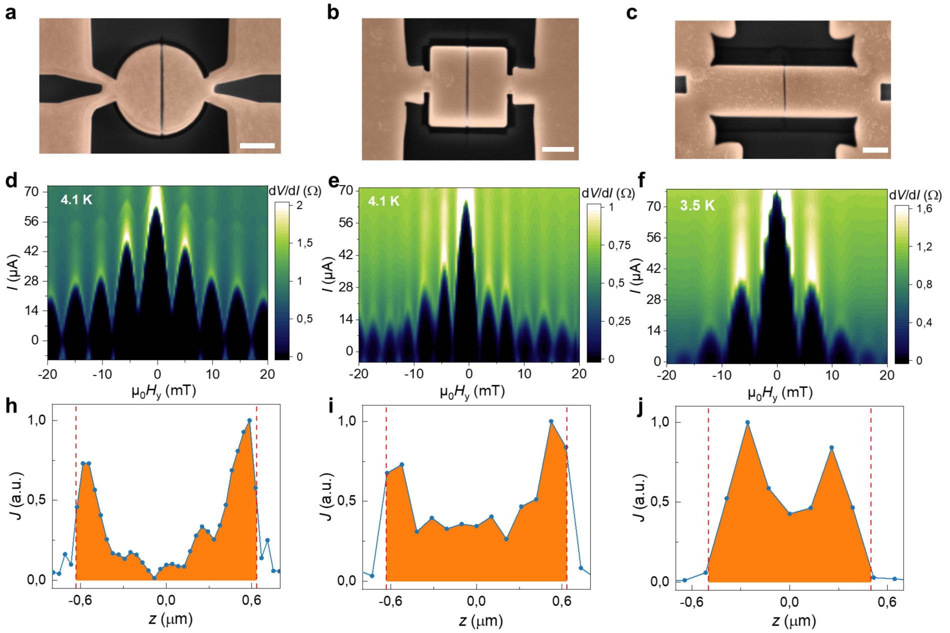

Figure 5.3: Spatial distribution of supercurrents versus geometry. (a-c) Top-view false-colored scanning electron micrographs of disk-shaped, square-shaped, and bar-shaped (3:1) devices. Here, the color indicates the NbTi/LSMO bilayer and all scale bars are equal to 500 nm. (d-f) Measured I$_c$(B$_\perp$)-patterns using a $B_\perp$ sweep. The color scale gives the differential resistance. (h-j) The results of Fourier analysis. The red-dashed lines indicate the size of the weak link.

the trench. Even in a 200 mT field, for which micromagnetic simulations demonstrate that the disk is fully magnetized, we find hardly any change in the two-channel I$_c$(B$_\perp$)-patterns (Fig. 5.4b,c). Note that we see small shifts in the central peaks with respect to zero out-of-plane field, but these are due to the misalignment between the sample plane and field direction.

We conclude from our IP field experiments that spin texture is not responsible for the proximity effect in our LSMO-based junctions. Specifically, the observed phenomena are very different from the observations in the Nb/Co disk junctions, where changes in spin texture lead to changes in I_c with fields of mT's, and where I_c is fully quenched when the disk becomes homogeneously magnetized. Here, $I_c(0)$ does not even decrease, emphasizing the robustness of the LRT supercurrents and indicating that the spin texture is not the LRT generator. Yet, the occurrence of the rim currents appears to be coupled to the geometry. In order to test this further, we reshaped a disk junction by cutting off one side. Interestingly, rim supercurrents remain on the curved side, but are absent on the flat side (see Appendix 5.5.4).

Since we ruled out spin texture, we conclude that there is a generator at play at,

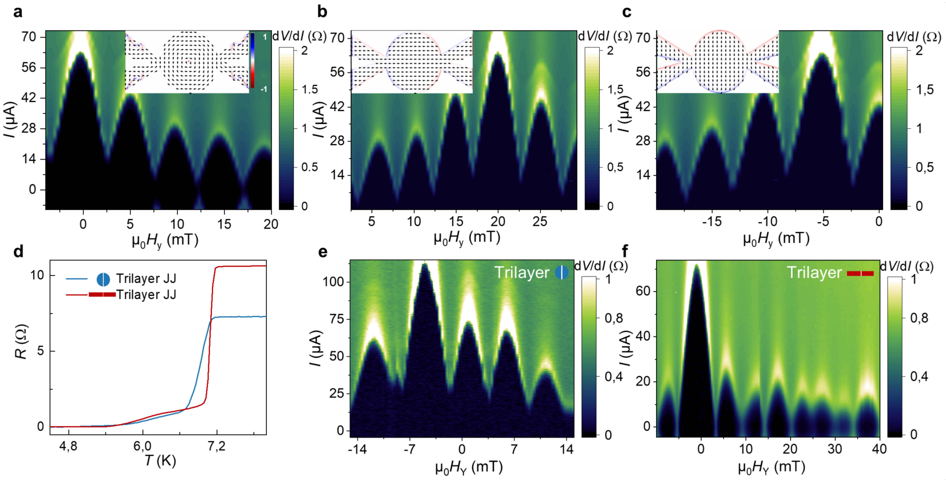

Figure 5.4: $I_c(B_\perp)$-patterns recorded on a disk-shaped bilayer junction under simultaneous application of IP fields (a-c) and $I_c(B_\perp)$-patterns recorded on trilayer junctions (d-f). (a) $I_c(B_\perp)$-pattern measured at zero IP field. The micromagnetic simulation in the inset demonstrates the LSMO disk has a ground state of a magnetic vortex. $I_c(B_\perp)$-patterns in the presence of 200 mT perpendicular (b) or parallel (c) to the trench. Accordingly, the insets display the fully-magnetized state in both cases. The color bar represents z components in the micromagnetic simulation. (d) RT curves of disk-shaped (blue) and bar-shaped (4:1) (red) NbTi/Ag/LSMO trilayer junctions. The corresponding $I_c(B_\perp)$-patterns, displayed in (e) and (f), are SQUID-like and Fraunhofer-like (f) at 4 K.

or close to, the LSMO/NbTi interface. In order to further investigate this, we fabricated junctions with an altered interface, by inserting a thin Ag layer (~ 10 nm). We find these junctions to retain their Josephson coupling and high critical current (see Fig. 5.4d-f). Besides, the NbTi/Ag/LSMO disk-junctions exhibit a two-channel-like $I_c(B_\perp)$-pattern, while the bar-shaped ones show a Fraunhofer pattern, as shown in Fig. 5.4e and f, respectively.

Finally, we paid special attention to small fields (~ 10 mT) when small motions of the vortex core are expected. We found no sign of a $0-\pi$ transition as observed in the Nb/Co system. This agrees with the predicted implication that such a transition cannot exist in a HMF [169]. More details are given in Appendix 5.5.4.

5.2.3. Dependence of I_c on temperature

One of the promises of supercurrents in HMFs is that the density can be very high, and therefore we measured $I_c(T)$ down to 1.5 K. Although I_c is well-defined at low temperatures, near the critical temperature the IV characteristics become rounded around I_c, which results in a slight ambiguity in determining I_c. The latter is believed to result from phase slips [48]. In this regime, we find I_c by fitting the IV curves to a model proposed by Ambegaokar and Halperin (AH) [170]. The values for I_c obtained this way are slightly different from the values extracted with a voltage criterion. More details are given in Appendix 5.5.6; the relevant IV characteristics are given in the Fig. 5.11. Also, we note that the fitting yields an average value for R_N of 0.8 Ω. This is significantly lower than the plateau in the $R(T)$ curve for this sample, which is around 2 Ω, indicating that the interface resistance is not small, and the interface is not very transparent.

The results for $I_c(T)$ are summarized Fig. 5.5. They show a parabolic dependence, and a current density $J_c = I_c/(d * L)$ of about 1.7×10^{10} A/m^2 at 1.5 K. If we consider that the currents mostly are confined to the rim of the disk, over a distance of ~ 200 nm, J_c is ~ 1.1×10^{11} A/m^2. Such high-density spin-polarized supercurrent holds promise for practical applications in superconducting spintronics.

Previously, $I_c(T)$ of HMF junctions were analyzed by an analogy to long diffusive SNS junctions [70, 171]. Here this analogy cannot be made, since the diffusive coherence length is roughly the size of the weak link. To show this, we estimate a mean free path ℓ_H of 6.5 nm [172] using the measured resistivity of LSMO (40 $\mu\Omega$cm). Next, using a Fermi velocity value $v_F \sim 7.4 \times 10^5$ m/s this leads to a diffusion constant $D = v_F * \ell_H/3$, and using $T_c = 5.5$ K, we find the diffusive coherence length $\xi_F = \sqrt{\hbar D/(2\pi k_B T_c)}$ to be ≈ 19 nm, which is roughly the size of the weak link. The same conclusion follows from considering the Thouless energy $E_{Th} = \hbar D/L^2$, which is about 2.6 meV, clearly larger than the gap Δ, which is 0.9 meV.

A theoretical framework for describing HMF-based junctions, which is more suited than the analogy to diffusive SNS junctions, was given in Refs. [72, 173]. For the clean case, the strength of I_c is determined by the two spin scattering channels ($\uparrow\downarrow - \downarrow\uparrow$) and ($\uparrow\uparrow$) from the superconductor to the half-metallic spin-up band. Close to T_c, $I_c(T)$ shows a (1-t)^2 dependence (with $t = T/T_c$), and a maximum at lower T, typically around $t = 0.2$. The maximum is robust, and is also predicted for long diffusive junctions [72], but has never been observed. In the current experiment, the data are well described by (1-t)^2, using $T_c = 5.5$ K, see Fig. 5.5. The experimentally lowest accessible temperature is 1.5 K, or $t = 0.3$, so the issue of the peak in I_c remains open.

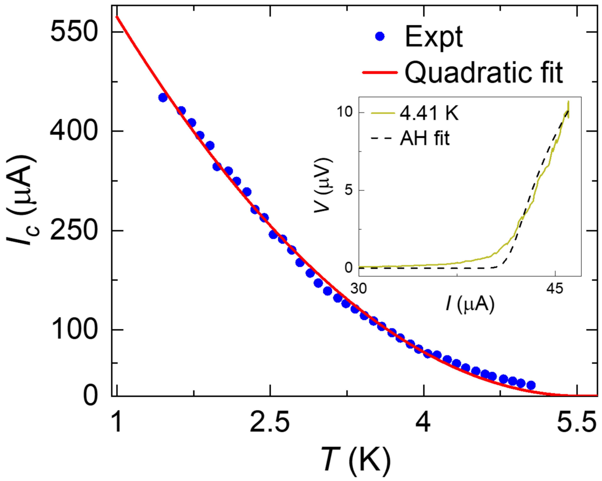

Figure 5.5: I_c as a function of temperature T. The inset shows how I_c values are obtained by fitting the IV curve (yellow) to the AH theory (black-dashed line) at 4.41 K, instead of being extracted with a voltage criterion. The extracted values of I_c are plotted by blue dots and well fitted by $(1\text{-}t)^2$ with $t = T/T_c$ (red line), with $T_c = 5.5$ K

5.3. Discussion

Above, we demonstrated the occurrence of a superconducting proximity effect in LSMO-based junctions of various shapes. In this section, we discuss the possible origin of the effect.

First note that the superconducting transport is carried by triplet Cooper pairs, as is indicated by the quite pure $(1-t)^2$ dependence of $I_c(t)$. For short junctions with a normal metal interlayer, the expected behavior is $1-t$ [174]. A quadratic dependence, or an upward curved behavior of $I_c(T)$, can in principle be found in S/N/S structures [175], but that would concern long junctions, whereas our junctions are in the short junction limit. We further discuss this point in Appendix 5.5.6.

Next, we find that the supercurrent generation is independent of the magnetic texture of the HMF. By applying in-plane fields, we observe the supercurrents to persist, even though the spin texture has been quenched. This suggests that another generator is at play for the triplets than the vortex magnetization pattern. A similar indication comes from the fact that homogeneously magnetized bar-shaped junctions show equally strong supercurrents.

Rejecting spin texture as the generator suggests that LRT correlations are instead generated at the NbTi/LSMO interface. This hypothesis is fully in line with research on the YBCO/LCMO and YBCO/LSMO systems. Visani, *et al*. reported supercurrents through 30 nm of LCMO between two layers of YBCO [148]. Very recently, Sanchez-Manzano, *et al*. found LRP effects in micrometer-long lateral junctions of LSMO with YBCO contacts. No engineered spin texture to generate triplets was utilized in either case. A possible source of LRT correlations could result from interfacial magnetism, possibly inhomogeneous in nature. Such mechanism actually exists at the YBCO/LCMO interface, due to exchange interactions over the Cu-O-Mn chains across the interface that lead to magnetic moment on the Cu [176]. However, since the samples fabricated from a NbTi/Ag/LSMO trilayer retain the same transport characteristics as the bilayer samples, the triplet generation in our NbTi/LSMO system is clearly not due to any orbital hybridization between NbTi and LSMO. Alternatively, this suggests that an intrinsic magnetic inhomogeneity in the LSMO top layer may be the generator. This could be formed in the growth procedure, if, for instance, the oxygen content in the top layer is reduced. That would lead to an increase in the amount of Mn^{3+} and shift the magnetism to a canted ferromagnetic insulating state [177]. Such a mechanism would also provide an explanation for LRT correlations in the LSMO/YBCO system.

Finally, we discuss the relation of the LRT generator to the highly confined triplet supercurrents at the rims of the disk-shaped devices. In the Nb/Co disk junctions studied before, these rim supercurrents were believed to be a direct result of the triplet nature of the supercurrents. Specifically, in the Nb/Co system the generator was identified as resulting from the synergistic effects of an effective SOI (provided by the vortex magnetization) and sample boundaries. This entails that LRT transport in the Nb/Co system can only emerge at the rims of the device, and consequently, rim supercurrents are very sensitive to in-plane fields. Contrarily, in the NbTi/LSMO system, triplets generation is independent of spin texture. Moreover, by modifying the geometry of the LSMO-based junctions, we see rim supercurrents appear in the disk and become weakened in the square and bar. Instead, the above results suggest rim supercurrents result from the combination between exotic triplet transport and the disk-shaped junction geometry, yet the driving mechanism remains to be further studied. We suspect that the difference between the Nb/Co and NbTi/LSMO systems is connected to the high spin polarization of the LSMO, where only one spin state can exist, but also this remains an open question.

5.4. Conclusion

In summary, we have unambiguously shown spin-polarized supercurrents and Josephson coupling in lateral NbTi/LSMO junctions with different geometries, and examined their origin. Surprisingly, these currents remain robust against large in-plane fields that are able to erase the spin texture, indicating that the spin texture is not relevant for producing such currents. From the unchanged results on devices fabricated from a NbTi/Ag/LSMO trilayer, we conclude that singlet to triplet conversion is not due to some interface coupling. Instead, intrinsic magnetic inhomogeneity in the LSMO top layer may be the key, which would also explain triplet generation in the LSMO/YBCO system. Finally, by performing Fourier analysis on the various $I_c(B_\perp)$-patterns, we find rim supercurrents in the disk-shaped junctions. The origin of these rim supercurrents is tied to the combination of triplet transport and disk-shaped junction geometry. However, their exact origin is currently left unexplained.

5.5. Appendix

5.5.1. Methods

Device fabrication: LSMO (40 nm) was deposited on a (001)-oriented $(LaAlO_3)_{0.3}(Sr_2TaAlO_6)_{0.7}$ (LSAT) crystal substrate at 700 ^{o}C in an off-axis sputtering system. The growth pressure was 0.7 mbar with Ar:O (3:2) mixing atmosphere. Information on the characterization of the LSMO films is given in Fig. 5.6. After cooling down to room temperature at a rate of 10 ^{o}C/min, the NbTi layer (60 nm) was deposited on LSMO $in\ situ$. The bilayer NbTi/LSMO was patterned through ebeam lithography and argon etching. Next, a focused ion beam (~ 30 pA) was utilized to structure the bilayer nanopattern. Especially, the trench with width ~ 20 nm was opened by using a small beam current (~ 1.5 pA). The depth of the trench was defined by the milling time. In the control experiments, we reduced and increased the milling time to get the NbTi and LSMO weak links (Fig. 5.7), respectively. Note the trilayer NbTi/Ag/LSMO devices were fabricated using the same recipe except for adjusting the milling time for making the trench.

Transport measurements: In a four-probe configuration, both the electrical transport and magnetoresistance were measured by using a lock-in setup. The frequency was set to 77.3 Hz for all the measurements. The resistance-temperature characteristics were taken with a 10 μA current in a cryostat (Oxford vector magnet). Direction-varying fields and a wide range of temperatures (300 K to 1.5 K) can be achieved in this cryostat. At the setpoint of temperature, the AC current was set to 1 μA as a background. The current vs voltage measurements were performed by sweeping a DC current superimposed on the background and reading the corresponding voltages, with a field sweep (yielding SQI patterns) or a temperature sweep (yielding $I_c(T)$).

Micromagnetic simulation: The micromagnetic simulations were conducted using a GPU-accelerated mumax3 [178]. The magnetization was set to 5.75×10^5 A/m, and exchange stiffness was 1.7×10^{-12} J/m, yielding an exchange length of $\ell_{ex} \approx$ 2.86 nm ($\ell_{ex} = \sqrt{2A_{ex}/\mu_0 M_s^2}$). According to Ref. [179], we consider a biaxial anisotropy in the LSMO(40 nm)/LSAT system. Therefore, the constant of biaxial anisotropy was set to 600 J/m^3. The damping constant was set to 0.5 artificially to get a high efficiency of convergence. To mimic the real situation, the arms were included in the simulation design.

5.5.2. Characterization of the epitaxy of LSMO films

LSMO films with a thickness of 40 nm were grown on LSAT substrates in an off-axis sputtering system. We employed different methods to examine and characterize the epitaxy of LSMO. Atomic force microscopy (AFM) was used to map the morphology of the films. As shown in Fig. 5.6a, clear atomic terraces were observed. Furthermore, x-ray diffraction (XRD) was used to verify the epitaxial growth of LSMO free of crystalline defects (Fig. 5.6b). Also, we measured the temperature-dependent resistivity of LSMO films using a Van de Pauw method. By calculating the temperature derivative of resistivity, The Curie temperature (T_c) was determined to be ~ 362 K (inset in Fig. 5.6c), consistent with the bulk value. The magnetic properties were measured by vibrating sample magnetometry (Fig. 5.6d). The coercive field was about 2.5 mT, and the saturation magnetization was calculated to be ~ 3.8 $\mu_B/f.u.$, in agreement with the theoretical value. Therefore, we conclude that the LSMO films used in this work are of high quality.

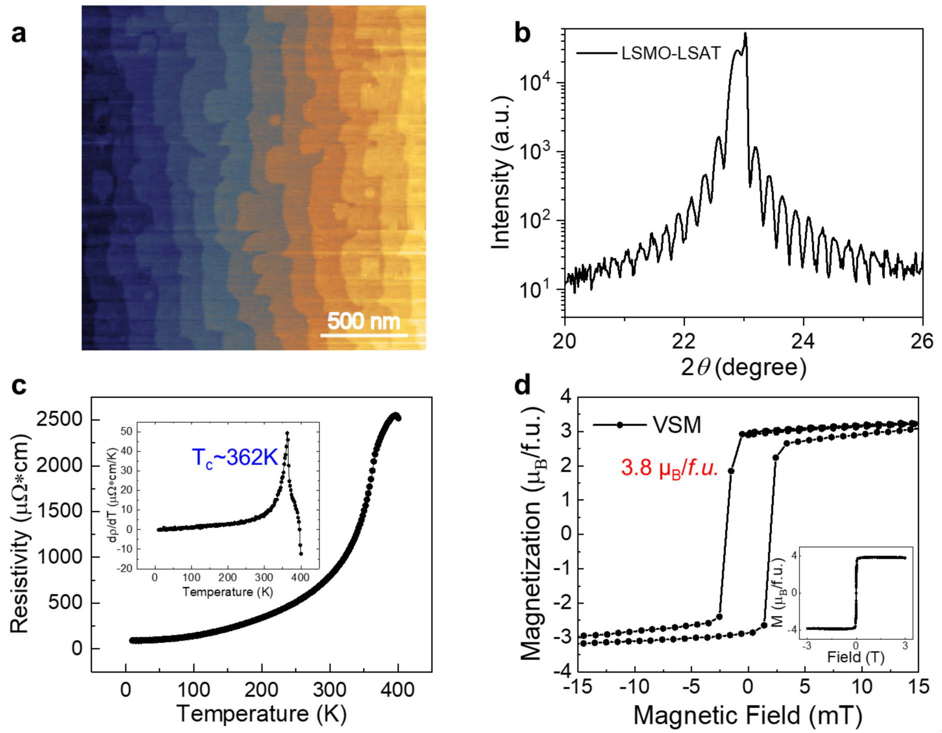

Figure 5.6: Property of epitaxial LSMO film. (a) AFM image of morphology of LSMO film. (b) XRD analysis at low-angel region. (c) Temperature-dependent resistivity characteristics. The inset shows the temperature derivative of resistivity to determine the Curie temperature T_c ~ 362 K. (d) Magnetization *vs* field curve obtained at 50 K. The inset is the full-range measurement with a field up to 3 T.

5.5.3. Junctions with shallow and deep trenches

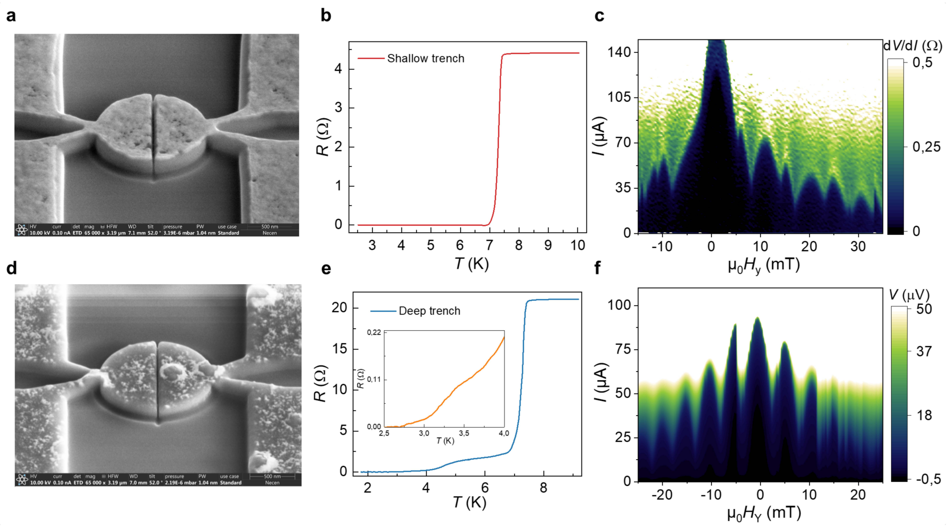

Figure 5.7: Characterizing NbTi/LSMO junctions with shallow and deep trenches. Front-view of SEM images of junctions with shallow (a) and deep (d) trenches. (b) and (e) corresponding RT curves. The inset in (e) is the magnification of the low-temperature region to clarify the second transition temperature. At 5.5 K, the measured SQI pattern of the junction with a shallow trench is Fraunhofer-like, while the junction with a deep trench exhibits a SQUID-like SQI pattern at 2.5 K, indicating rim supercurrents only appear in a disk-shaped ferromagnetic weak link. Note that a shallow trench means the weak link is NbTi.

5.5.4. Analyzing SQI patterns

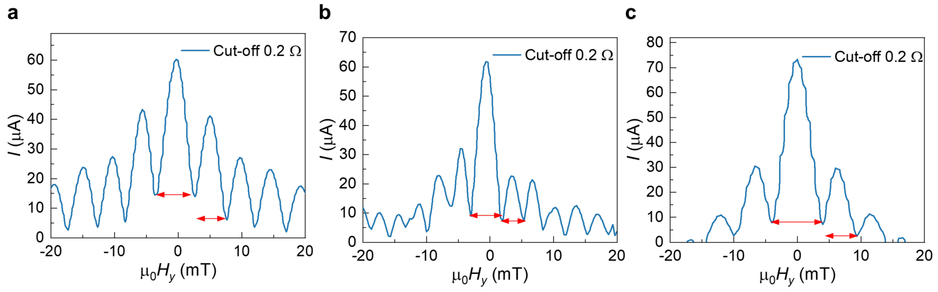

Figure 5.8: Plot of the extracted critical current with a resistance criterion for the disk-shaped (a), square-shaped (b), and bar-shaped (c) NbTi/LSMO junctions, corresponding to Fig. 5.3 in the main text.

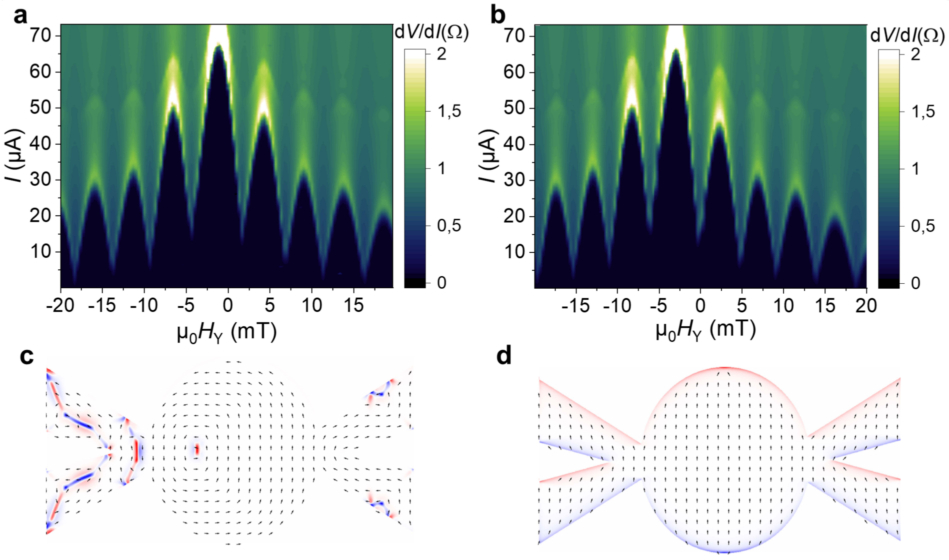

Figure 5.9: Measured SQI patterns with constant IP field 10 mT (a) and 100 mT (b) along the trench at 4.1 K. No change in both the amplitude and period of the SQI patterns is observed. The shift of the central peak with respect to the zero field is due to the misalignment between the sample and IP fields. (c) and (d) are the simulated magnetization states, correspondingly.

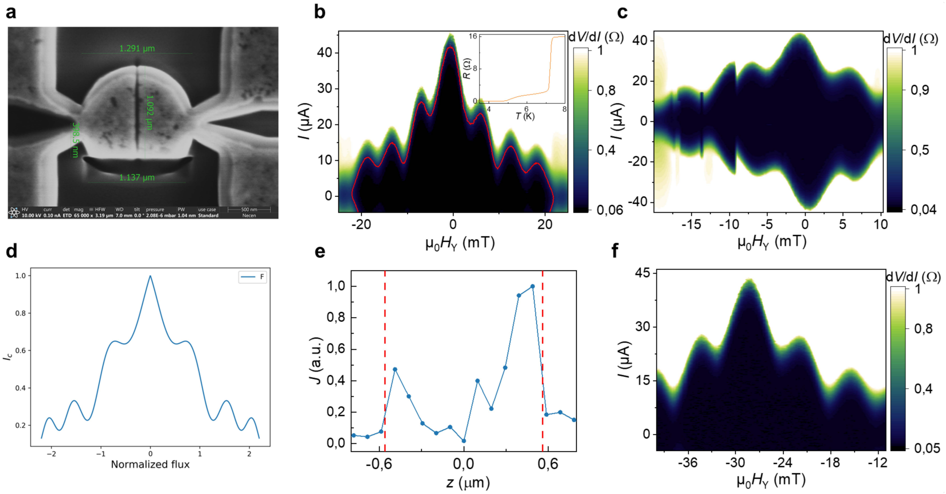

Figure 5.10: (a) Top-view SEM image of an irregular disk. (b) SQI pattern measured at 4.1 K. The red curve is the plot of the critical current that is extracted with a resistance criterion of 0.2 Ω. The inset shows the RT curve of the junction. (c) SQI pattern with sweeping current positively and negatively. (d) Simulated critical current as a function of magnetic flux quanta. (e) Fourier analysis on the SQI pattern (b) with a resistance criterion. (f) SQI pattern in the presence of IP 200 mT field.

5.5.5. A disk-shaped NbTi/LSMO junction with a flat side

Having seen no effect of the IP fields on the triplet supercurrents (Fig. 5.4), we reshape the LSMO disk by cutting off one side and thus acquire an irregular geometry of the LSMO-based junction (Fig. 5.10). Consequently, the pure magnetic vortex will not be the ground state, and local stray fields can occur. In Fig. 5.10b, the obtained SQI pattern becomes quite abnormal with non-zero minima. By determining both the positive and the negative critical current, we see that the SQI pattern is asymmetric (Fig. 5.10c). Moreover, the ratio between the period of the central peak and that of the first lobe has increased significantly, to ~ 1.59. Börcsök, $et\ al.$ [66] modeled the complex Fraunhofer patterns arising from a non-homogeneous magnetization inside the barrier, in particular when it is larger at the edges of a magnetic Josephson junction. Using Eq. 9 in Ref. [180], we show a qualitative calculation in Fig. 5.10d with $p = 0.2$, $Q = -1$, and $q = 3$, though a quantitative fitting is not obtained due to the irregular geometry of this junction. The simulated curve is analogous to the measured critical current upon the out-of-plane field (red curve in Fig. 5.10b). Interestingly, we still see rim supercurrents on one side in this case. On the other side, the rim supercurrents are largely suppressed, according to the Fourier analysis(Fig. 5.10e). We again apply IP fields (~ 200 mT) to saturate the magnetization of this junction. As shown in Fig. 5.10f, the measured SQI pattern does not change, indicating the transport of triplet supercurrents is intrinsic in the variously shaped NbTi/LSMO junctions, regardless of the magnetization states.

5.5.6. Determining I_c and calculating E_{Th}

At high temperatures, all IV curves have pronounced rounding features at $I \sim I_c$ due to phase slippage, leading to ambiguity in determining I_c [48]. Following Ambegaokar and Halperin [170], we calculate the IV curves analytically giving

$$V = \frac{2I_cR_N}{\gamma_0}\frac{e^{\pi\gamma_0 i}-1}{e^{\pi\gamma_0 i}}\left\{\int_0^{2\pi} e^{-\pi\gamma_0\varphi/2} I_0(\gamma_0 sin\frac{\varphi}{2})d\varphi\right\}^{-1} \tag{5.1}$$

where $\gamma_0 = \Phi_0 I_c/\pi k_B T$, $i = I/I_c$. I_c is the critical current, R_N is the normal resistance, I_0 represents a modified Bessel function. The simulated results are shown in Fig. 5.11b. As γ_0 becomes large enough, meaning the Josephson coupling energy is comparable to the thermal energy, the rounding feature is significantly suppressed. Shifting the baselines of the IV curves to zero by subtracting the minimum of each IV curve individually, we then fit the measured IV to Eq. 5.1 and determine I_c analytically (Fig. 5.11c). We obtain an average $R_N \approx 0.8\ \Omega$. The fitted I_c is slightly larger than the extracted I_c with a resistance criterion.

Next, we discuss the I_c versus temperature. In the main text, we argued that a de-

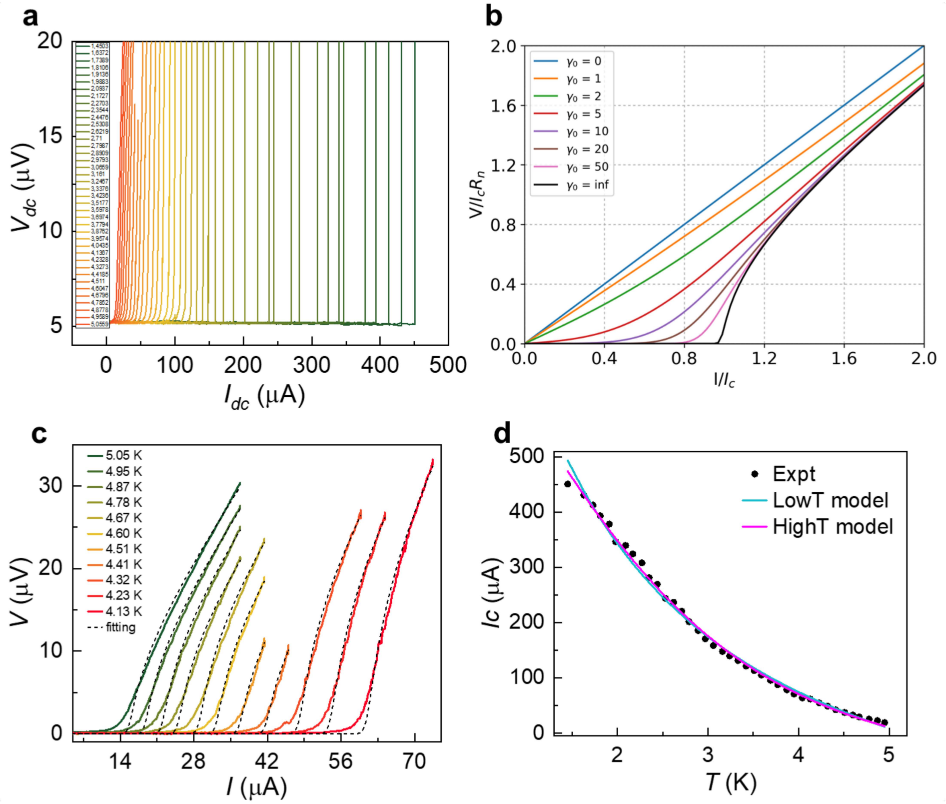

Figure 5.11: Determining I_c and calculating E_{Th}. (a) Raw IV curves. (b) Simulated IV curves based on the AH theory, Eq. 5.1, for different values of $\gamma_0 = \Phi_o I_c/(\pi k_B T)$. (c) Measured IV curves at high temperatures and the corresponding fit (black dashed line) using Eq. 5.1. (d) A plot of the fitted I_c as a function of temperature and fits using Eq. 5.2 (cyan curve) and Eq. 5.3 (magenta curve).

scription that assumes the diffusive and long regime of a mesoscopic junction, such as used in Refs. [14, 171, 181], is not valid. Here, a diffusive and long junction means $\ell_H < d$ and $\Delta > E_{Th}$. Unlike the YBCO/LSMO system, in which $k_B T \gg E_{Th}$ [14], the second transition temperature of the NbTi/LSMO junction is quite low ~ 5.2 K. First we therefore fit the temperature dependence of I_c to Eq. 5.1 in the low-temperature limit ($k_B T \ll E_{Th}$), according to Ref. [171],

$$\frac{eR_N I_c}{E_{Th}} = a(1 - be^{-aE_{Th}/3.2k_B T}) \tag{5.2}$$

where the coefficients a and b are 10.82 and 1.30, respectively. k_B is the Boltzmann constant, and T represents temperature. The result of the fit is shown in Fig. 5.11d (cyan line) and at first sight looks good. However, the resulting $E_{Th} \approx 34.6$ μeV, is much smaller than $k_B T$ (~ 353 μeV at 4.1 K). The fitted R_N is 0.37 Ω and unreasonable, in view of both the residual resistance in the RT curve (Fig. 5.2) and the fitted data with the AH theory.

Therefore, we consider the high-temperature case ($\mathrm{k}_B T \gg E_{Th}$) and fit the temperature-dependent I_c to

$$eR_N I_c = 64\pi k_B T \sum_{n=0}^{\infty} \frac{L}{L_{\omega_n}} \frac{\Delta^2 \exp^{-L/L_{\omega_n}}}{[\omega_n + \Omega_n + \sqrt{2(\Omega_n^2 + \omega_n \Omega_n)}]^2} \tag{5.3}$$

where L is the length of the junction (d in the main text), $L_{\omega_n} = \sqrt{\hbar D/2\omega_n}$, $\omega_n = (2n+1)\pi k_B T$ is the Matsubara frequency, $\Omega_n = \sqrt{\Delta^2 + \omega_n^2}$. The fitting curve (magenta) is plotted in Fig. 5.11d. From this fit, we find E_{Th} to be about 112 μeV, the fitted Δ is 788 μeV, and T_c is 5.27 K. The ratio $E_{Th}/\Delta(0)$ is therefore 0.14. The fitted R_N is about 0.87 Ω, coincident with the fitting results with the AH theory. According to $\Delta(0) = 1.764 k_B T_c$ [182], we obtain $\Delta(0) \approx 790$ μeV, which is in agreement with the fitted Δ. In order to show better what the high-temperature looks like, we simulate the temperature-dependent characteristic $I_c R_N$ voltage based on Eq. 5.3 and plot I_c (in appropriate units) versus T/T_c for various values of $E_{Th}/\Delta(0)$ in Fig. 5.12. The case of our fit is the green line (a ratio of 0.15), clearly starting off quadratically. The plateau is reached at $T/T_c \approx 0.6$, corresponding to ~ 300 mK in the experiment.

We still argue, however, that this description is unphysical. In the diffusive regime we have $\xi_F = \sqrt{\hbar D/2\pi k_B T_c} \approx 19$ nm with $T_c = 5.5$ K. Therefore, the junction length d nearly equals ξ_F. Then, $E_{Th} = \hbar D/L^2 \approx 2.6$ meV, which is clearly larger than $\Delta \approx 0.9$ meV. In other words, there is a strong discrepancy between the calculated (diffusive) value of E_{Th} and the fitted result. We conclude, not surprisingly, that the long diffusive junction limit cannot be valid. Instead, given $\ell_H < d$ and $E_{Th} > \Delta$, we are in the short regime, where our I_c data are (well) well described by $(1 - T/T_c)^2$, as seen in Fig. 5.5. Further quantitative analysis of $I_c(T)$ of half-metallic Josephson junction may need rigorous theoretical study.

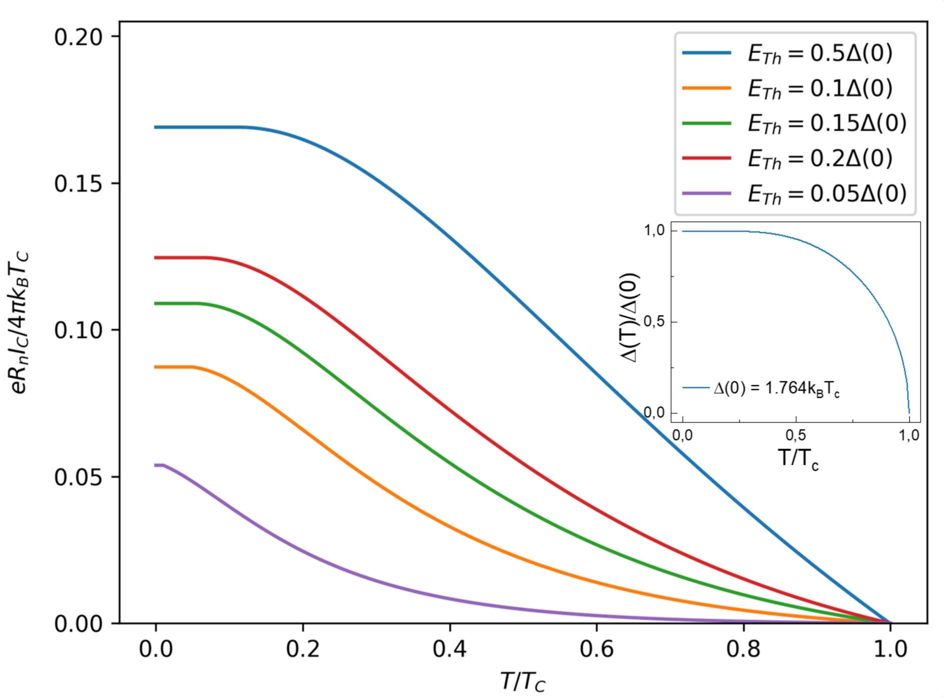

Figure 5.12: Simulated temperature dependence of the product of eI_cR_N at various ratios of $E_{Th}/\Delta(0)$ based on Eq. 5.3. The inset shows the universal $\Delta(T)/\Delta(0)$ as a function of T/T_c, in which $\Delta(0) = 1.764k_BT_c$ [182].